Reviews on Advanced Materials and Technologies, 2025, vol. 7, no. 3, pp. 184–197
DOI: 10.17586/2687-0568-2025-7-3-184-197

Impact of Brazed Joint Defects on Operability of ITER Divertor Dome Plasma Facing Units

A. Rybikov [1,2,*], A. Eremkin [1], A. Komarov [1], V. Kuznetsov [1], A. Volodin [1], P. Piskarev [1], I. Bogdanov [1], V. Tanchuk [1], S. Grigoriev [1], M. Dorogov [2], N. Arkhipov [3]

[1] JSC «NIIEFA» (Efremov Institute), Doroga na Metallostroy, 3, Metallostroy, St. Petersburg, 196641, Russia
[2] Institute of Advanced Data Transfer Systems, ITMO University, Kronverkskiy pr., 49, lit. A, St. Petersburg, 197101, Russia
[3] Institution «Project Center ITER», Raspletina St., 11, bldg. 2, Moscow, 123182, Russia

Article history

Received September 09, 2025
Received in revised form, September 29, 2025
Accepted September 30, 2025
Available online September 31, 2025

Abstract

The study presents the results of numerical simulation and experiments of thermal processes in the mock-ups of the ITER divertor dome plasma facing units (PFU). The divertor is a critical component subjected to extreme thermal loads which imposes high requirements on the reliability of its PFUs. The purpose of the study is to assess the impact of the parameters (geometry, size, localization) of defects in the brazed joint of tungsten-copper armour and bronze heat sink under heat loads q_s = 1–6 MW/m^2. The simulation by the finite-element method was performed for the PFU configurations with defects of various shapes and sizes. The results were compared with the experimental data of thermal tests. It was found that an increase in the defect size leads to an increase in the armour temperature: at the maximum defect area (50% of the joint area), the local temperature increases by 55%, and the average temperature by 40% (q_s = 6 MW/m^2). The defect shape (rectangular/triangular) has a minor effect: deviations do not exceed 1.4% for the maximum and 10% for the average values. The longitudinal castellation (electrical discharge machining) of tiles in the model can affect the temperature distribution. The maximum armour surface temperature for all versions did not exceed 1200 °C. At loads ≤ 4 MW/m^2, cooling remains convective, while at the higher loads, local boiling zones occur without transition to a critical heat flux. The comparison between the calculated and experimental results has detected the similarity in the temperature distributions.

Keywords: Divertor dome; Plasma facing unit; Brazing defect; Thermal tests; Castellation

1. INTRODUCTION

The ITER divertor consists of 54 demountable cassettes each of which includes a supporting structure (cassette body) and three components with PFU sets: the inner vertical target, the outer vertical target and the dome involving the umbrella, inner particle reflector plate and outer particle reflector plate [1–8]. These components are located at the intersection of magnetic field lines where high-energy plasma particles directly interact with the material surface and produce extreme thermal and radiation loads.

The plasma facing armour of the divertor will be completely made of tungsten, a refractory metal with a melting point of 3422 °C and with the maximum interatomic bonding strength. Tungsten was selected due to its properties: low coefficient of physical sputtering, high thermal conductivity (167 W/(m·K) at 25 °C), low coefficient of thermal expansion ($4.67 \cdot 10^{-6}$ K^{-1}), heat resistance, high modulus of elasticity, corrosion resistance and chemical inertness [9–12]. These characteristics make tungsten a nearly irreplaceable material suitable for use under the extreme thermal loads up to 20 MW/m^2 at slow transient processes in plasma lasting about 10 seconds.

To minimize thermomechanical stresses due to the incompatibility of temperature deformations at the interface between the tungsten armour and the bronze heat sink caused by a difference in the thermal expansion coefficients of these materials by more than three times, an intermediate layer technique is used. Soft oxygen-free copper with a high thermal conductivity is used as a buffer material which is applied on the tungsten surface by a melting method. The thickness of the specified intermedi-

* Corresponding author: A. Rybikov, e-mail: rybikov@sintez.niiefa.spb.su

ate layer which ensures a gradient redistribution of stresses during thermal cycles is 1–2 mm [13].

The ITER divertor PFUs will be affected by deuterium and tritium ions, their fusion products (helium atoms and free neutrons), as well as impurity particles deposited on the vessel walls [14–16]. During plasma disruptions, these high-energy particles can heat the component surface to extremely high temperatures which leads to the thermal fatigue of the materials as one of the most important damaging mechanisms.

To reduce the peak thermal loads on the divertor armour to an acceptable level of 5–10 MW/m^2, the divertor operation in the (complete or partial) detachment mode is considered. In this mode, the charged particle flux which reaches the divertor surface is significantly reduced: plasma is as if detached from the receiving plates, and the power coming to the wall layer from the central plasma reaches their surface mainly in the form of radiation and kinetic energy of neutral particles. Photons and neutrals are not confined by the magnetic field; therefore, the related energy flux is distributed over the surface more uniformly [16].

The production of the divertor components is a complex manufacturing problem due to the properties of the materials used. The technology of joining the tungsten-copper (W-Cu) armour tiles with the bronze substrates of water-cooled heat sinks is particularly problematic. The quality of such joints directly affects the heat transfer and, consequently, the temperature modes of operation of the PFUs [1,13].

The study [17] specifies the maximum acceptable defects (size, shape, location) when brazing the bimetal tungsten-copper armour tiles to the water-cooled heat sinks of the ITER divertor. It was found that the defects with an area up to 40% of the brazed joint (Cu/CuCrZr) do not result in the critical reduction of the component performance at specified cyclic thermal loads. The aim of work [17] was to elaborate the acceptance criteria for the joints based on ultrasonic testing (UT) data; furthermore, the examined defects were due to manufacturing and were not related to post-brazing damages.

To ensure the performance and durability of the ITER divertor dome PFUs, it is of the highest importance to evaluate the effect of the joint defects on the thermomechanical behavior of the structure. The defects in the joints may substantially impair the heat transfer which will lead to local overheating of the armour and to the possible rupture of material. The defects in the copper sublayer and the tungsten-copper armour joint may occur both under the specified operating conditions of the thermonuclear reactor and during the experimental (thermal) simulation of these processes.

The presented study is focused on the comprehensive assessment of the impact of the defect parameters (geometry, size, localization) in the joints at the thermal loads 1–6 MW/m^2 including the load of 5 MW/m^2 which is specified for the operation of the divertor components. These defects simulate delamination of the copper sublayer which may take place during the thermal tests with a surface thermal load [14,15,18].

To carry out experiments on the ITER divertor components, the JSC “NIIEFA” built a special ITER divertor test facility (IDTF) which allows simulating heat fluxes corresponding to actual operating conditions [19]. The test results are supplemented by the numerical simulation using the ANSYS software which makes it possible to obtain the comprehensive information on the thermomechanical behavior of the tested structures.

The study of the ITER divertor dome PFUs is of a fundamental importance for the operability and safety of the future thermonuclear reactor. Understanding the mechanisms of the impact of the defects in the joints on the thermal processes will allow, if necessary, to optimize the design and manufacturing technology for the divertor components, as well as to improve their reliability and to extend their lifetime under the extreme thermal loads.

2. CALCULATION MODEL

The free-of-defect geometric model of the Dome PFU mock-up is a bimetal steel-bronze substrate: the upper part is CuCrZr bronze heat sink and the lower part is 316L(N)-IG stainless steel (SS) base. The W-Cu armour tiles are brazed onto the PFU in two longitudinal rows, 13 tiles each. Two front armour tiles have a straight cut at an angle of 20° to the vertical. Inside the PFU there is a water-cooling channel the upper part of which is made in the form of a hypervapotron [1,2,13,17,18]. Coolant (water) inlet/outlet pipes of the cooling system manifolds (removed from the calculation model) are connected to the PFUs from below on the both ends of the mock-up.

In addition to the free-of-defect model of the PFU mock-up, two versions of this model were considered with defects in the joints between the copper substrates of the W armour and the bronze heat sink in the brazing area. These models have serial numbers PFU 040 p08 (Fig. 1a) and PFU 035 p03 (Fig. 1b). In the PFU 035 p03 model, the longitudinal castellation of W tiles was additionally made in the ratio of 1:1 for each tile, and the castellation gap thickness is 0.3 mm. The castellation is understood to be the electrical discharge machining of the bimetal W-Cu tile surface involving the formation of oriented grooves which improve the heat sink characteristics of the PFU.

The rectangular and triangular defects of various areas and spatial positions were introduced into the calculation models of the brazing area for armour tile rows A and B (PFU 035 p03) and C и D (PFU 040 p08), with the number of tiles in each row varying from 1 up to 13 (Fig. 2). The defects for the specified versions are the gaps in the brazing area on the joints of the Cu substrates

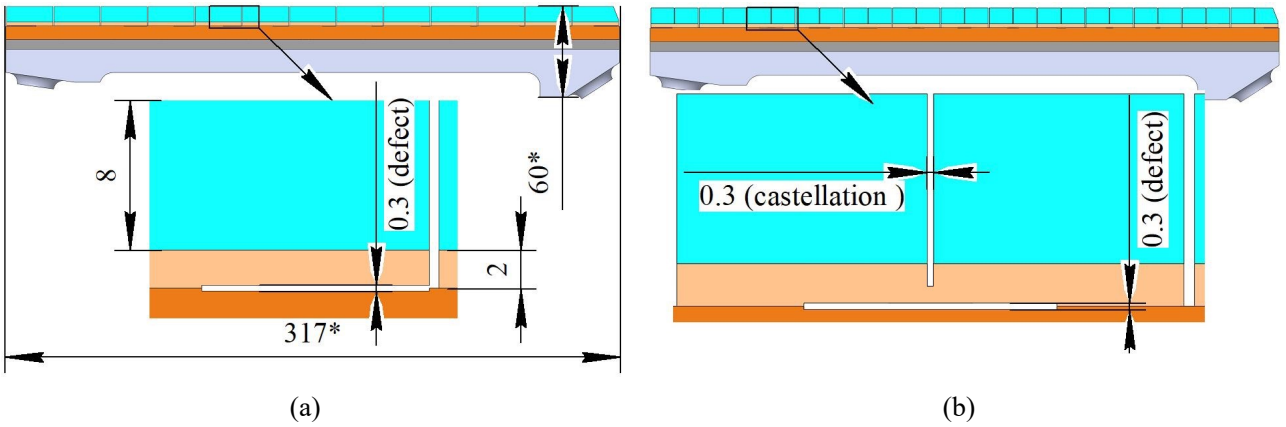

Fig. 1. Defect location under the dome PFU armour after brazing: (a) PFU 040 p08, (b) PFU 035 p03.

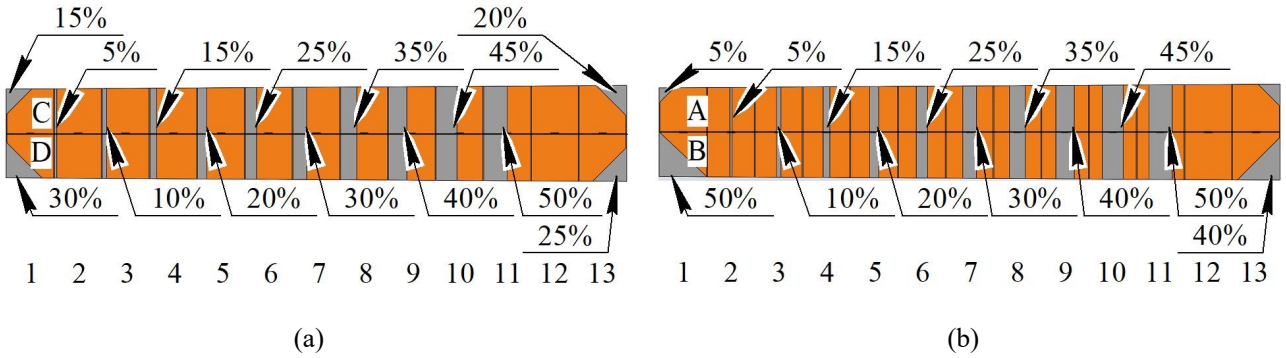

Fig. 2. Defect arrangement (quantity and place) under the dome PFU armour after brazing: (a) PFU 040 p08, (b) PFU 035 p03.

and the bronze heat sink with a total thickness of 0.3 mm, 0.15 mm of which is Cu and remaining 0.15 mm is bronze. Figure 2 shows the arrangement of the defects in the W-Cu joints in the horizontal longitudinal cross-section for the both mock-up versions with defects. The defects under the edge tiles on both sides are located at the outer corners of the mock-up and have a triangular shape, while the defects under the remaining tiles are located along the width of the mock-up and have a rectangular shape. The defect area sizes in the both versions and for the both shapes vary from 5 to 50% of relevant initial areas of the joints between the Cu substrates and the bronze heat sink. Meanwhile, in the PFU 035 p03 model, the rectangular defects are located in the middle of the joint surfaces of the Cu substrates, and in the PFU 040 p08 model they lie along the edge of the joint surface, on one side.

For the specified models, finite-element calculation meshes were constructed with dimensions of 3.3 million elements for the initial free-of-defect model, 4.7 million elements for the PFU 035 p03 model and 4.4 million elements for the PFU 040 p08 model.

The finite element calculations were performed using the ANSYS 2019 R3 software (thermal module Mechanical APDL), which is certified for numerical simulations within the ITER project. The problem statement represented a simulation of thermal testing of divertor element mock-ups exposed to plasma, taking into account the physical conditions of the experimental tests. Thermal loads were applied as specified surface heat fluxes from the electron beam gun, and convective heat removal by the water flow inside the cooling channels was modeled through the heat transfer coefficient and water temperature. Adiabatic boundary conditions were applied on unspecified surfaces, and radiative heat exchange with the environment was considered negligible.

Volumetric finite elements SOLID70 were used to solve the three-dimensional heat conduction problem, having one degree of freedom—the temperature. Surface finite elements SURF152 were applied to represent boundary conditions including prescribed temperature, heat flux, convective heat transfer, and radiation. Mesh convergence was verified on local model fragments, resulting in an optimal cell size of approximately 50–100 microns near the cooled surfaces, balancing numerical accuracy and computational cost.

The material parameters used in solving the problem in the steady-state mode included only thermal conductivity, the values of which for each material are presented in the article (Fig. 3), while the properties of the coolant (water) were based on classical reference data.

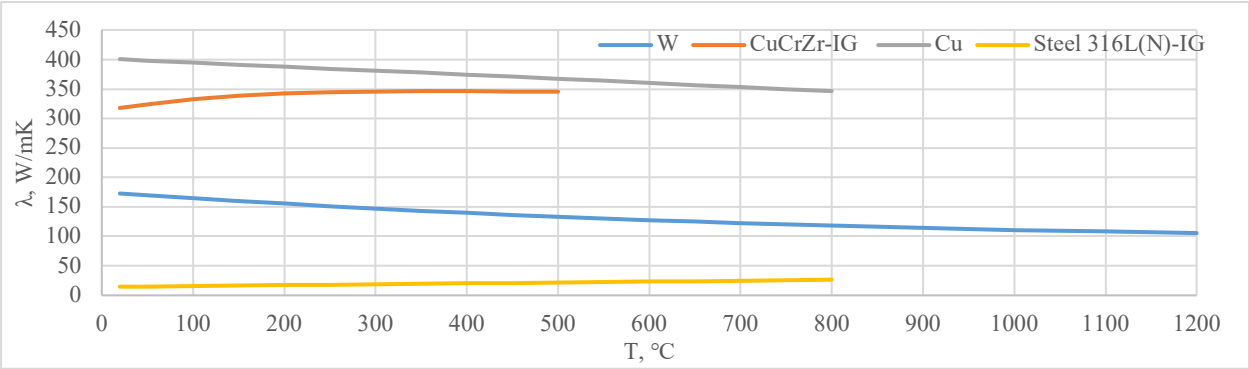

Fig. 3. Thermal conductivity-temperature plot for tungsten, bronze, CuCrZr-IG, copper, 316L steel.

Special attention was given to modeling thermal contact at the defect interfaces: since the experiments were conducted in vacuum and direct thermal contact was absent, radiative heat transfer across the narrow gaps between copper and bronze interfaces was modeled by introducing fictitious thin layers with equivalent thermal conductivity. This approach ensured equivalence between the radiative heat flux and the artificially introduced conductive property, thus not assuming the interfaces as perfect thermal insulators.

Figure 3 shows the dependence of thermal conductivity on the temperature of the materials of the mock-up components used in the calculations (W, Cu, bronze and SS) [20–23].

Figure 4 presents boundary conditions for the thermal calculations. A given constant value of heat load density q_s [MW/m^2] is set on the open outer surfaces of the armour tiles; the study considers the range 1–6 MW/m^2 of values q_s (Fig. 4, in red). On the cooling channel surface (Fig. 4, highlighted in blue), the condition of convection heat exchange with the cooling water flow is set. The value of convection heat flux is specified through the value of convection heat transfer coefficient α [W/(m^2·K)] and the water flow temperature T_{bulk} [°C]. The heat transfer coefficient is specified as dependent on the cooling channel surface temperature T_{ws} [°C] in the form of a boiling curve (Fig. 5), the shape of which depends in turn on the hydraulic diameter of the cooling channel D_h [mm], as well as on the pressure P [bar], velocity v [m/s] and temperature T_{bulk} of the water flow in the cooling channel. The hydraulic diameter D_h for all calculation versions is specified as the $4 \cdot S_h / \Pi_h$ ratio (S_h is the hydraulic cross-section area [mm^2], Π_h is the wetted perimeter of the hydraulic cross-section [mm]) and is equal to 16 mm (cross-section) with a minimum area of the hydraulic cross-section ($S_{h,min}$ = 448 mm^2, $\Pi_{h,min}$ = 11.2 mm). The water flow pressure p is also assumed to be the same for all calculation versions and is equal to the inlet water pressure P_{in} = 39 bar (38.5 atm); the water pressure loss in the cooling channel is only 6 kPa (0.15% of P_{in}). The water flow

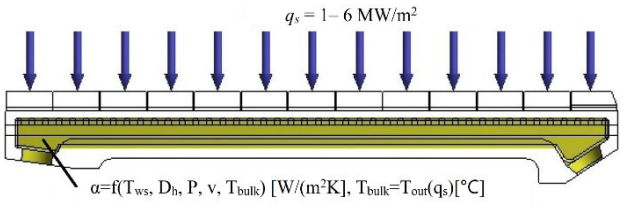

Fig. 4. Boundary conditions for thermal calculations: convection flux in the hypervapotron and heat flux on the PFU surface.

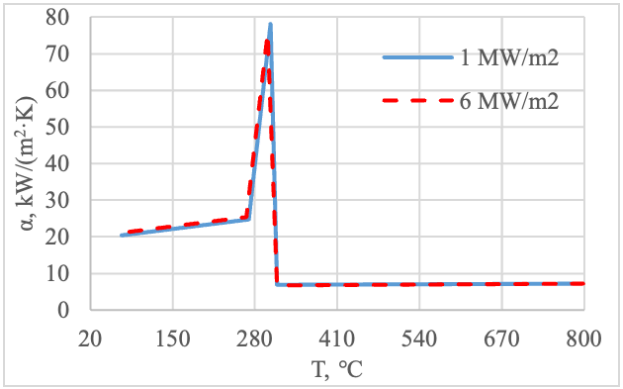

Fig. 5. Boiling curves for versions q_s=1 MW/m^2 (v=4.2 m/s, D_h=16 mm, P=39 bar, T_{bulk}=72 °C) and q_s=6 MW/m^2 (v=4.2 m/s, D_h=16 mm, P=39 bar, T_{bulk}=82 °C).

velocity v is determined through the specified water flow rate in the cooling channel G = 1.84 kg/s and is equal to 4.2 m/s by formula $v = G/(\rho \cdot S_{h,min})$ (ρ = 977.7 kg/m^3 is the water density at 70 °C). The water flow temperature T_{bulk} is given equal to the outlet water temperature $T_{out} = T_{in} + \Delta T$, where ΔT is maximum water heating during the water flow through the mock-up cooling channel, which is determined by formula $\Delta T = Q / (G \cdot C_P)$ (C_P = 4180 J/(kg·K) is the heat capacity of water at 70 °C), where the integral heat release power Q is determined as $q_s \cdot S_{load}$, where $S_{load} = 317.5 \cdot (49.2 + 45.5) / 2 = 15033.625$ mm^2 is the area of heat load absorption by the mock-up armour. Table 1 presents the dependencies of the outlet water temperature T_{out} and the maximum water heating ΔT on q_s. As Figure 5 shows, there are slight differences between the boiling

Table 1. Integral heat release power, maximum water heating and outlet water temperature in the cooling channel at various heat load surface densities.

Heat load surface density, MW/m^2	Integral heat release power, kW	Maximum water heating, °C	Outlet water temperature, °C
1	15.03	2	72
2	30.07	4	74
3	45.1	6	76
4	60.13	8	78
5	75.17	10	80
6	90.2	12	82

curves for q_s = 1 MW/m^2 and q_s =6 MW/m^2, and the maximum difference between the curves at the critical heat flux point is no more than 5%. The boiling curves for intermediate heat loads (q_s = 2÷5 MW/m^2) are located between them, therefore, they are not shown in Figure 5.

3. ARMOUR BRAZING DEFECTS AND ULTRASONIC TESTING OF THEIR SHAPE AND SIZE

After the deposition of the STEMET® 1108 alloy on the bronze heat sink, each W-Cu tile was mounted, followed by the paired fixation of the tiles using a patented pressing device with a gas bellows [1,2,17,18,23,24]. The PFU was assembled in a heat-resistant tooling and then was placed in a vacuum resistance furnace. The thermal process of brazing combined with the heat treatment of bronze involved brazing and aging.

After armour brazing, the defects were made in the brazing area using the electrical discharge machine. The defects were located similar to those of the calculation model. The cutting thickness was 0.3–0.45 mm in the brazed joints of the copper substrates and the bronze heat sink, with a thickness of 0.15 ± 0.07 mm for copper and 0.15 ± 0.07 mm for bronze.

Similar to the calculation models, in the experimental models the brazing areas of the armour tile rows are designated A_m and B_m (PFU 035 p03) and C_m and D_m (PFU 040 p08); the number of tiles in each row is from 1 up to 13, and the rectangular and triangular defects of various areas and spatial positions are introduced (Fig. 6).

After the defects were made, the UT of the brazed joint was performed to monitor the shape and size of the introduced defects. An analysis of ultrasonic defectograms has detected discrepancies between the actual sizes of the defects and the data obtained as a result of the UT. Systematic differences between the measured and actual UT data were found in both tested groups of mock-ups, and the total number of significant deviations was 48, 12 in each row. The most pronounced discrepancies were observed in PFU 035 p03, especially at the initial testing points which is due to the impact of the edge defects. In PFU 040 p08, the moderate but significant deviations were registered with the maximum differences at the middle testing points. It should be considered that due to the edge effects of ultrasound propagation, the UT does not allow detecting the defects of W-Cu and Cu-CuCrZr joints located at the distance of less than 1 mm from the edges of the armour tile which reduces the size of edge defects.

4. THERMAL TESTS

Thermal tests of the PFUs were carried out at the IDTF test facility [19]. This test facility is an electron beam complex constructed for thermal cycling tests of the ITER divertor components to be supplied not only by the Russian Federation but also by other countries participating in the ITER project. The IDTF test facility (Fig. 7a) consists of a test-

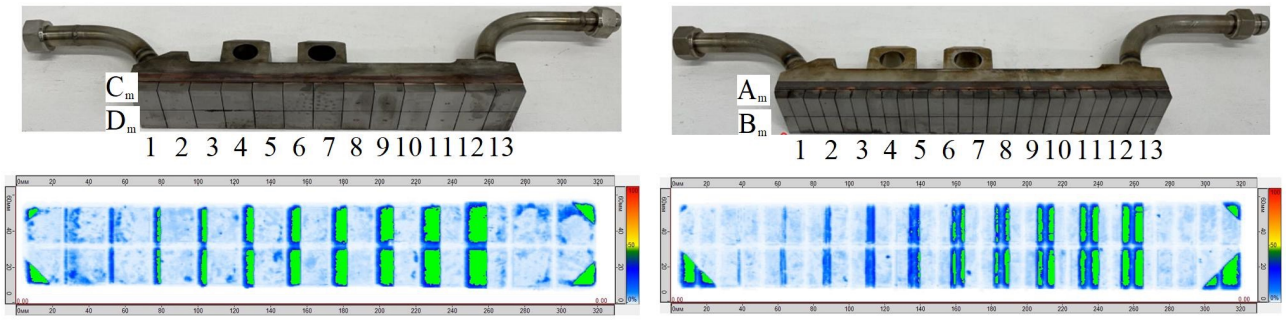

(a) (b)

Fig. 6. Defect appearance and UT defectograms of defect location after brazing under the dome PFU armour: (a) PFU 040 p08, (b) PFU 035 p03.

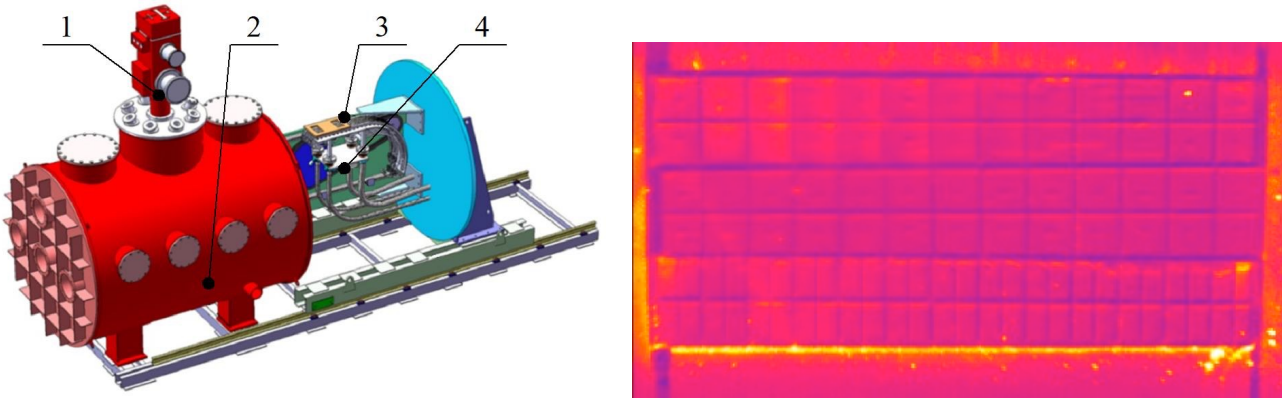

Fig. 7. IDTF test facility. (a) IDTF model: 1 – electron beam gun, 2 – vacuum chamber, 3 – test object, 4 – target device. (b) Mock-up on the target device of IDTF test facility.

ing vacuum chamber with a pumping system, an electron beam system (EBS) with a maximum power of 800 kW, target cooling circuits and other auxiliary systems, and experimental data acquisition equipment. The EBS is served as the source of thermal cycling load on the test objects. An electron beam with an energy up to 60 keV interacts with the metal surface of the test object, with much of the kinetic energy being converted into thermal energy which is the surface heat load. This thermal energy is released in the surface layer several microns thick. Using the magnetic deflection system of the EBS, the electron beam travels along the test object surface in a programmed path and warms up the required area. By controlling the power and magnetic deflection system of the EBS, it is possible to apply the surface heat load of the required density. The mode of surface heat load switching between two identical loading areas is often used. In this case, the EBS operates continuously in the constant power mode, and the electron beam jumps from one area to another.

The mock-up with three dome PFUs, two of which had defects in the brazing area, was installed on the target device of the IDTF and connected to the water-cooling circuit of the target. The free-of-defect PFU mock-up was located in the center, and the rows were designated as "No defect". Then, a map of mock-up armour surface emissivity was obtained using an infrared imager. To obtain the map, the mock-up was uniformly heated with cooling water up to 70 °C without application of the surface heat load. As mentioned above, the armour tile surface emissivity map makes it possible to adjust the readings of the infrared imager during the thermal tests.

The mock-up armour surface was surrounded by four copper water-cooled masks protecting the target device of the test facility from the side parts of the electron beam raster.

The thermal tests of this mock-up consisted of a gradual thermal mapping with a step variation in the absorbed power density from 1 to 6 MW/m^2. Upon attaining each successive value of this parameter, an infrared image was recorded using the infrared imager. Figures 7b, 9b and 12b show the examples of this image.

The power generated by the scanning electron beam was preset prior to each stage of the thermal tests. The specific thermal power q_{abs} absorbed by the heat loading area was measured by the water calorimetry and calculated by formula

$$q_{abs} = P_{abs} / S = Qc\Delta T / S \ \ [\mathrm{MW/m^2}],$$

where Q is the mass flow rate of cooling water, c is the specific heat capacity of water, $\Delta T = T_2 - T_1$ [°C], T_2 is the cooling water temperature at the mock-up outlet, T_1 is the cooling water temperature at the mock-up inlet, S is the heat loading area. The cooling water parameters and the calculation of the absorbed power density were recorded continuously during all tests.

The parameters of mock-up cooling water during the thermal tests were in accordance with those specified in the relevant procedure and were maintained as follows: the water flow rate through the mock-up 4.35 kg/s, the mock-up inlet temperature 70 ± 10 °C, and the pressure 39 ± 0.5 bar.

The analysis of thermodynamic parameters of the PFU 040 p08 and PFU 035 p03 models under different heat fluxes (from 1 to 6 MW/m²) has detected a consistent increase in average and maximum temperatures both in the absence of the defects and in their presence (Fig. 8). The most pronounced increase in the maximum temperatures is typical for the models with defects during the thermal tests.

Figure 8 shows the results of the dependencies of the average and maximum temperatures with/without defects on the heat loads. The temperature designations are given in Table 2.

Table 2. Designations of calculated and experimental, average and maximum temperatures used in Fig. 8.

Parameter	PFU 040 p08	PFU 035 p03
Calculated average temperature, with no defects	T_avg_calc_no_def_040	T_avg_calc_no_def_035
Calculated average temperature, with defects	T_avg_calc_def_040	T_avg_calc_def_035
Experimental average temperature, with no defects	T_avg_exp_no_def_040	T_avg_exp_no_def_035
Experimental average temperature, with defects	T_avg_exp_def_040	T_avg_exp_def_035
Calculated maximum temperature, with no defects	T_max_calc_no_def_040	T_max_calc_no_def_035
Calculated maximum temperature, with defects	T_max_calc_def_040	T_max_calc_def_035
Experimental maximum temperature, with no defects	T_max_exp_no_def_040	T_max_exp_no_def_035
Experimental maximum temperature, with defects	T_max_exp_def_040	T_max_exp_def_035

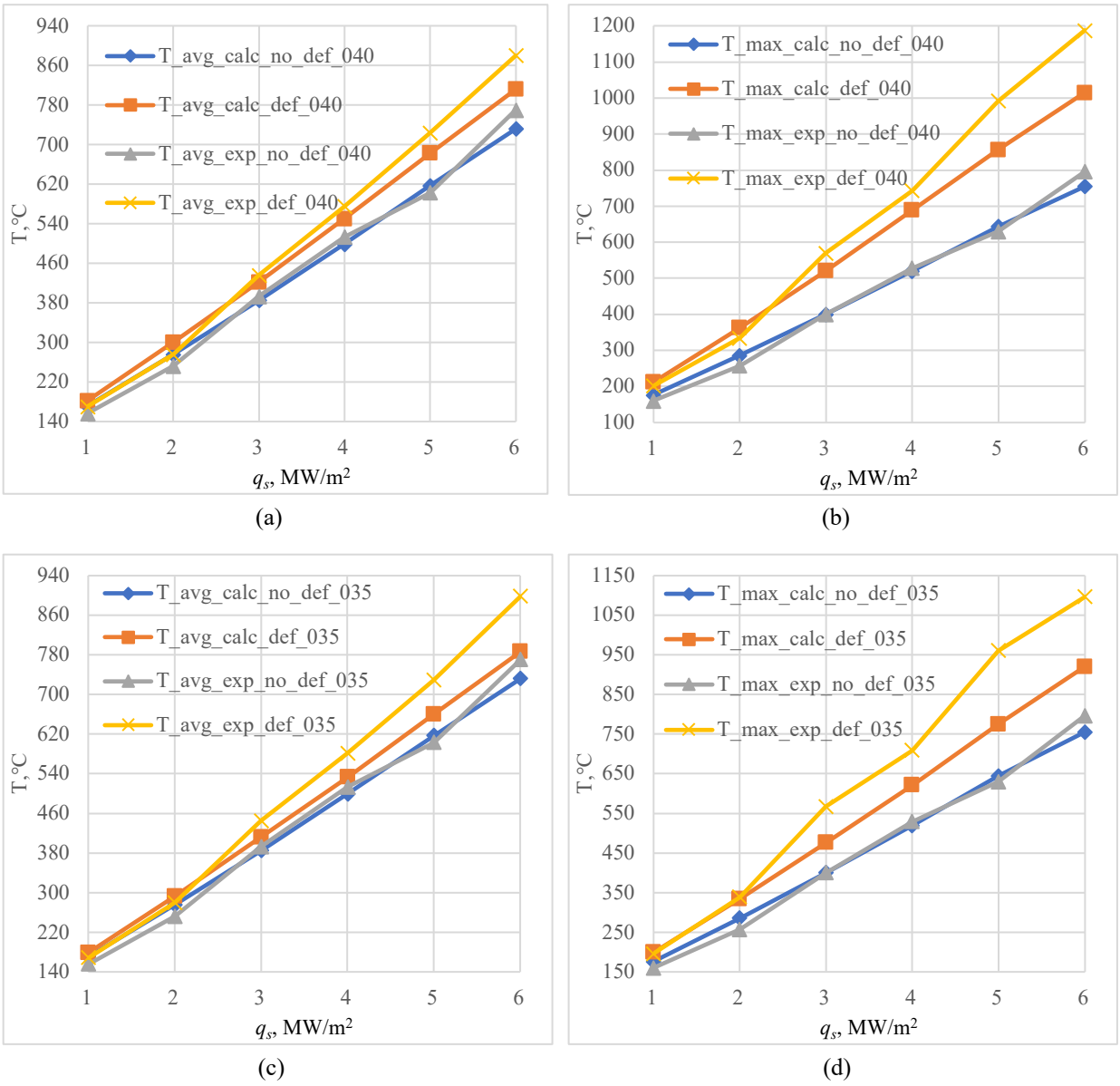

Fig. 8. Dependences of the average and maximum temperatures with/without defects on heat loads: (a) average calculated and experimental temperatures for PFU 040 p08; (b) average calculated and experimental temperatures for PFU 035 p03; (c) maximum calculated and experimental temperatures for PFU 040 p08; (d) maximum calculated and experimental temperatures for PFU 035 p03.

With an increasing heat load, a stable growth of the average values of the maximum temperatures is observed: from 171 °C to 733–770 °C for the mock-ups with no defects, and from 182 °C to 812–898 °C for the mock-ups with defects. The maximum temperatures for the mock-ups reach 755–796 °C and 920–1188 °C

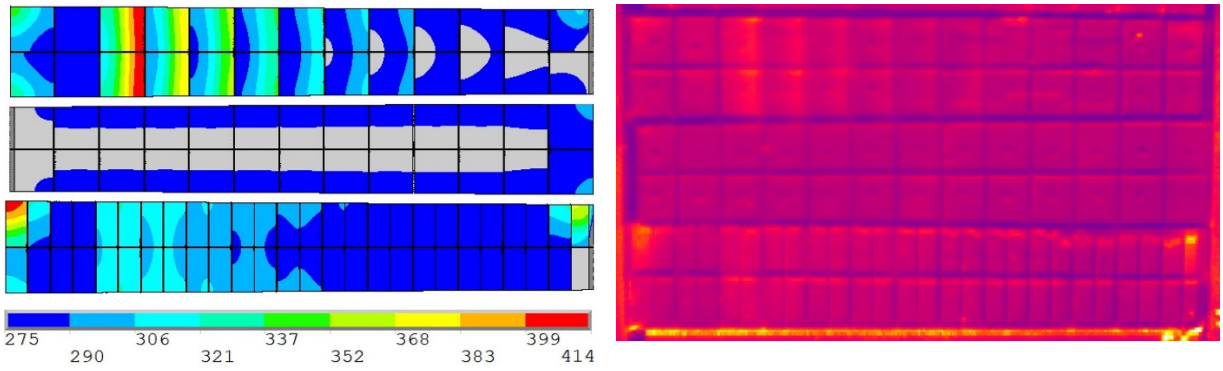

(a) (b)

Fig. 9. Stationary temperature [°C] distribution over the PFU mock-ups in all versions at q_s = 2 MW/m^2: (a) calculation models, top – PFU 040 p08, center – model with no defects, bottom – PFU 035 p03; (b) experimental models – arrangement similar to (a).

Table 3. Designations of maximum calculated and experimental temperatures (with/without defects) used in Figs. 10, 11, 13, 14.

Parameter	PFU 040 p08	PFU 035 p03	No defects
Calculated maximum temperature, the upper tile row	C	A	No_calc_def_up
Calculated maximum temperature, the lower tile row	D	B	No_calc_def_down
Experimental maximum temperature, the upper tile row	Cm	Am	No_exp_def_up
Experimental maximum temperature, the lower tile row	Dm	Bm	No_exp_def_down

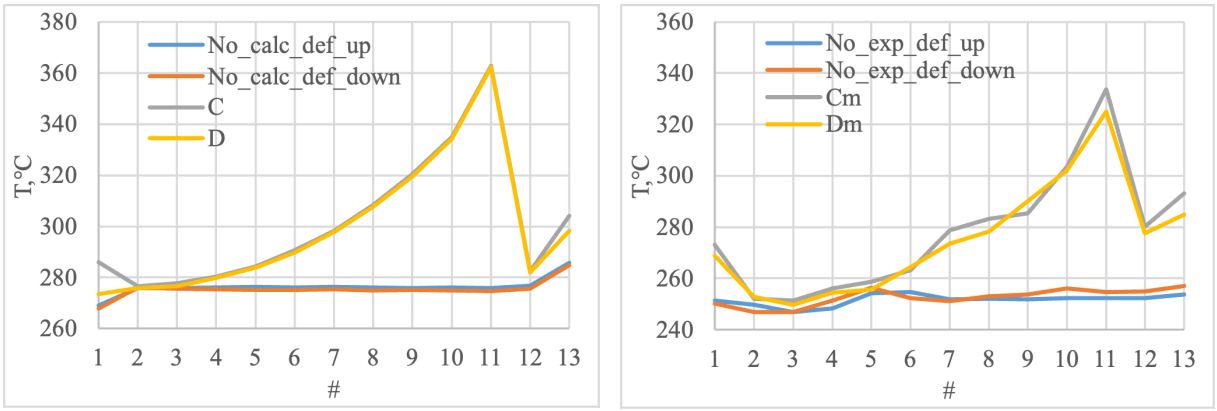

(a) (b)

Fig. 10. Maximum temperature distribution plots for the thermal loaded surfaces of the tiles for the PFU 040 p08 model and for the model with no defects at q_s = 2 MW/m^2: (a) thermal calculation; (b) bench tests.

without and with defects, respectively, while the bench tests record not only higher peak (maximum defect area) but also slightly lower average temperatures as compared to the thermal calculations. The PFU 040 p08 model demonstrates the higher maximum temperatures as compared to the PFU 035 p03 model (Fig. 8c,d). The defects multiply the thermal values. The data indicate a good correlation between the calculated and experimental values at all levels of the heat load, thus confirming the reliability of the selected models and thermal analysis techniques.

The calculated and experimental stationary temperature distributions over the surface of the PFU tiles are presented in Figures 9–14, and the temperature designations are given in Table 3.

Thus, the analysis of thermodynamic parameters of the PFU 040 P08 and PFU 035 P03 models under the different heat loads demonstrates that both the average and the maximum temperatures grow with the increasing heat flux, with the presence of defects contributing to a significant increase in the maximum temperatures. The bench tests confirm the tendencies of the thermal calculation and show the slightly underestimated values of the average temperatures and the highest peak temperatures which indicates the influence of the actual operating conditions on the heat load and temperature distribution.

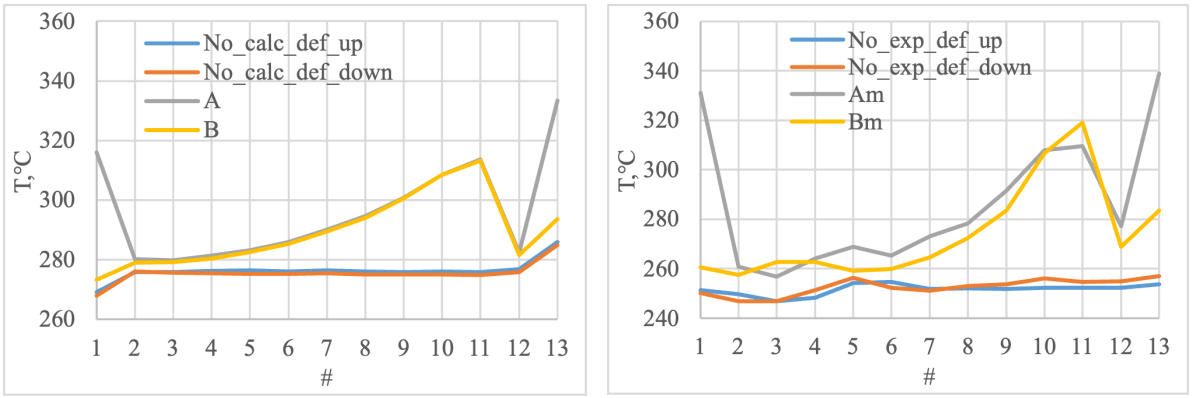

Fig. 11. Maximum temperature distribution plots for the thermal loaded surfaces of the tiles for the PFU 035 p03 model and for the model with no defects at q_s = 2 MW/m^2: (a) thermal calculation; (b) bench tests.

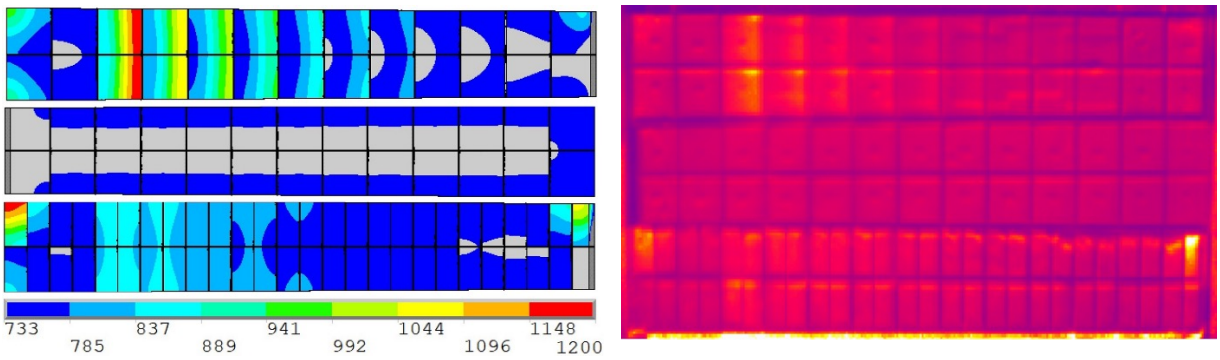

Fig. 12. Stationary temperature [ºC] distribution over the PFU mock-ups in all versions at q_s =6 MW/m^2: a) calculation models, top – PFU 040 P08, center – model with no defects, bottom – PFU 035 p03; b) experimental models – arrangement similar to (a).

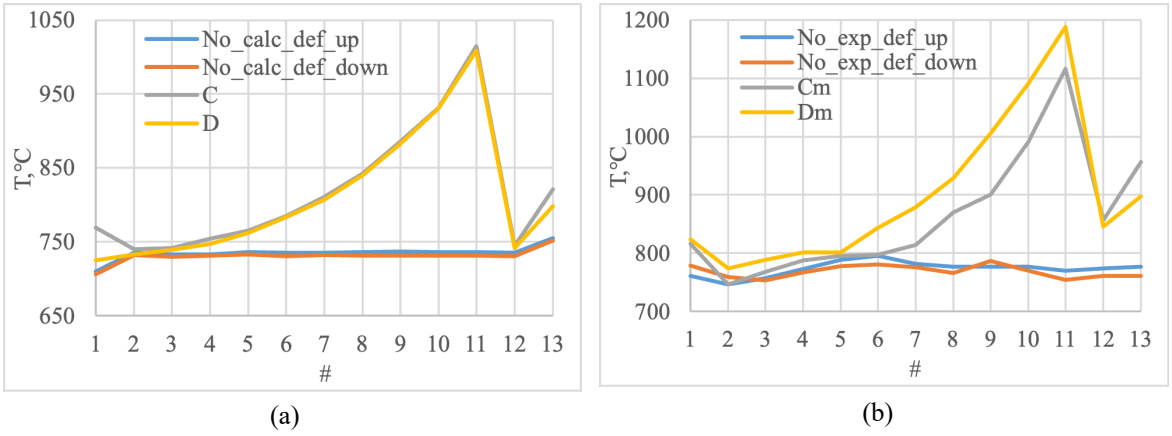

Fig. 13. Maximum temperature distribution plots for the thermal loaded surfaces of the tiles for the PFU 040 p08 model and for the model with no defects at q_s = 6 MW/m^2: (a) thermal calculation; (b) bench tests.

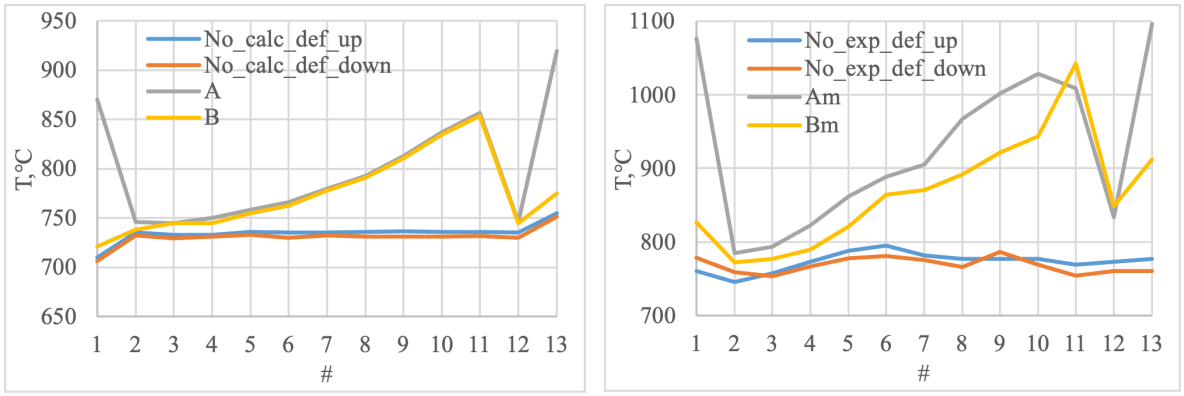

Fig. 14. Maximum temperature distribution plots for the thermal loaded surfaces of the tiles for the PFU 035 p03 model and for the model with no defects at q_s = 6 MW/m^2: (a) thermal calculation; (b) bench tests.

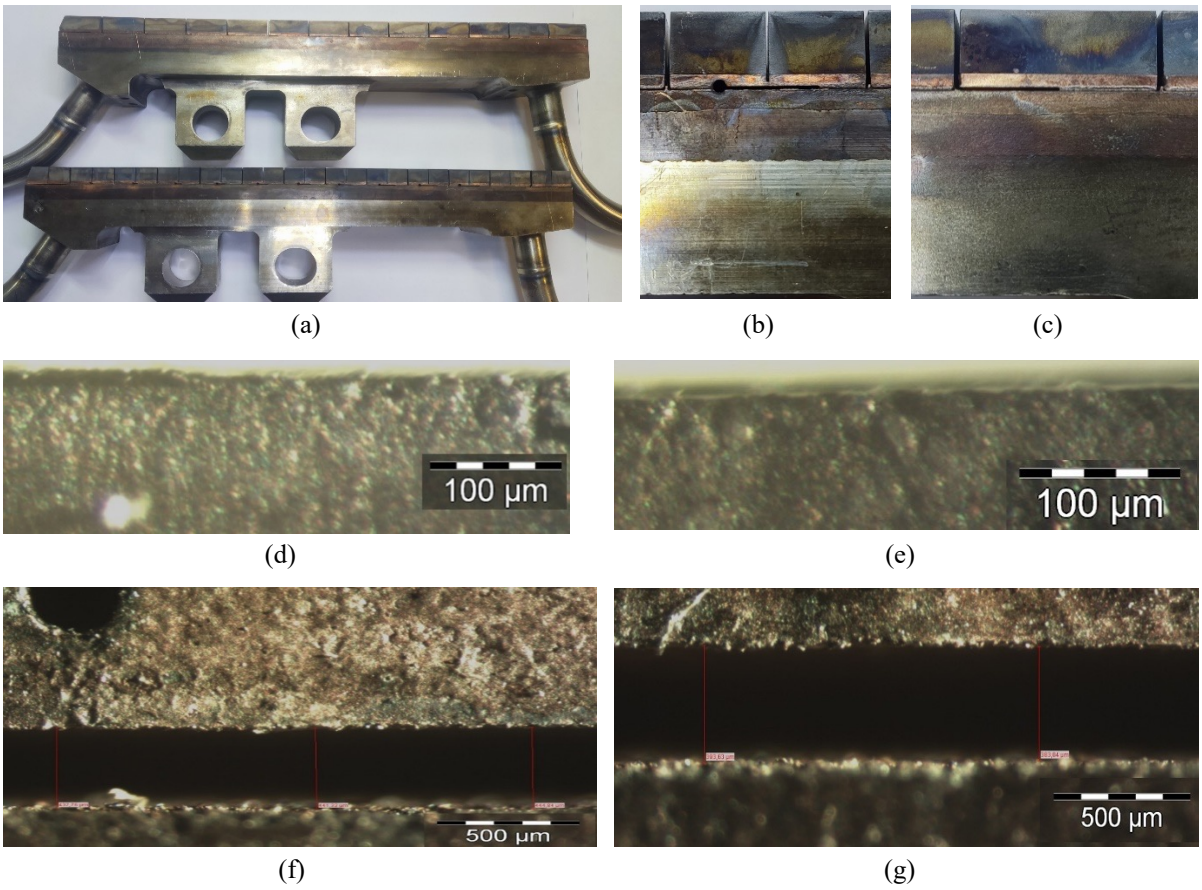

Fig. 15. PFU defects: (a) PFU 040 p08 (bottom) and PFU 035 p03 (top); (b) close-up view of the PFU 040 p08 area in tile row # 11, 50% defect; (c) close-up view of the PFU 035 p03 area in tile row #11, 50% defect; (d) tungsten side surface on the edge, above the PFU 035 p03 defect zone; (e) tungsten side surface on the edge, above the PFU 040 p08 defect zone, (f) side surface of the defect zone in the PFU 035 p03 brazed joint; (g) side surface of the defect zone in the PFU 040 p08 brazed joint.

5. OPTICAL MICROSCOPY

The examination was performed using an optical microscope (Olympus SZX16). A tungsten surface was examined above the largest defect # 11-50% for PFU 035 p03 (Fig. 15b,d,f) and PFU 040 p08 (Fig. 15c,e,g). No marks of near-surface tungsten melting or cracking were detected. Actual measurements of cutting zone defects were also carried out after the tests. Neither geometry changes, nor reduction/broadening of the cutting zone was found.

6. ANALYSIS OF THERMAL CHARACTERISTICS OF PFU MOCK-UPS WITH DEFECTS UNDER VARIOUS HEAT LOADS

The presented data demonstrate the comprehensive study of the temperature distribution on the surfaces of the PFU mock-up tiles with different defect types. The analysis shows a substantial impact of artificial defects in the joints of the W-Cu armour and the bronze heat sink on the thermal characteristics of the models. With an increase in the heat load from 1 to 6 MW/m^2, a nonlinear temperature growth is observed, especially in the models with defects. Significant differences between the calculated and experimental data indicate the difficulty of accurate simulation of heat transfer in systems with defects which emphasizes the importance of experiments.

When analyzing the presented data, it is evident that the models with defects consistently demonstrate higher temperatures as compared to the models with no defects at all heat loads. The relatively uniform temperature distribution along the PFU surface is typical for the models with no defects, while the models with defects show significant temperature peaks, especially in the positions corresponding to the location of the maximum defects. For the PFU 040 p08 model at the heat load of 1 MW/m^2, the temperature of 212 °C (thermal calculation) was recorded in position # 11 (50% defect), while for the free-of-defect model the average temperature was 171 °C and the maximum temperature in position # 13 was 176 °C. When increasing the load to 4 MW/m^2, the gap between the temperatures in the defect zone and the average values of the free-of-defect model becomes wider: the temperature attains 689 °C (thermal calculation) for position # 11 with defects against the average temperature of 499 °C for that without defects which corresponds to the difference of 190 °C (38.2%).

For the PFU 035 p03 model, where the defects are located in the center, the temperature peaks are less pronounced as compared to the PFU 040 p08 model, where the defects are located at the edges of the joint surface. For example, at 4 MW/m^2, the maximum temperature in position # 13 (defects) for PFU 035 p03 is 621 °C (thermal calculation), while for PFU 040 p08 under similar conditions, the maximum temperature in the same position is 689 °C. This emphasizes that not only the size of the defect but also its localization affects the thermal distribution.

The differences persist during the bench tests. For instance, at 4 MW/m^2, the PFU 040 p08 model with defects in position # 11 demonstrates 743 °C, and the PFU 035 p03 model in position # 1 – 709 °C which confirms more intense overheating of the edge defects. Thus, the defect position affects the formation of local temperature anomalies, especially under high heat loads.

With a growing heat load, a significant increase in the temperature gradient between the tile surface areas is observed, particularly in the models with defects. For example, for PFU 040 p08 at q_s = 1 MW/m^2, the difference between the maximum temperature in the defect zone (212 °C, position # 11) and the average temperature of the model with no defects (171 °C) is about 41 °C. However, at q_s = 4 MW/m^2 this gradient sharply grows: the maximum temperature reaches 689 °C in the model with defects (position # 11), while the average temperature for the model without defects is 499 °C, which corresponds to the difference of 190 °C. For PFU 035 p03 at the similar load, the gap between the maximum temperature in position # 13 (621 °C) and the average temperature of the model with no defects (499 °C) is 122 °C.

At the load over 2 MW/m^2, the defects not only provoke general overheating but also form temperature contrasts. For instance, for PFU 040 p08 at q_s = 6 MW/m^2 during the bench tests, the difference between the maximum temperature in position # 11 (1188 °C) and the average temperature of the model with no defects (733 °C) attains 455 °C. For PFU 035 p03 at the same load, the difference between 1096 °C (position # 13) and 771 °C (average value, with defects) is 325 °C.

The defects, particularly located at the edges of the joint surfaces, create the areas of intense thermal stress. Such discontinuities can accelerate the degradation of materials, reduce the strength of joints and increase the risk of critical failures which must be considered during the design and operation of the components.

The bench tests have detected the underestimation of temperatures in the calculation models, particularly pronounced at the high loads (4–6 MW/m^2). For PFU 040 p08 with defects at 6 MW/m^2, the discrepancy between the calculated and experimental average temperatures was 68 °C (812 °C vs 880 °C), and for PFU 035 p03—112 °C (786 °C vs 898 °C). This indicates the need to consider the additional factors in the experimental models, such as imperfect joints and nonuniform heat removal.

The heat load growth from 1 to 6 MW/m^2 is accompanied by a non-linear increase in the temperature difference between the defect and free-of-defect mock-ups. For PFU 040 p08, the gap between the average values increases from 11 °C (1 MW/m^2) to 110 °C (6 MW/m^2), and for PFU 035 p03—from 8 °C to 127 °C. The maximum peaks increase exponentially: for PFU 040 p08 from 212 °C to 1188 °C, and for PFU 035 p03—from 199 °C to 1096 °C, which emphasizes the crucial importance of defect monitoring in the enhanced heat flux modes.

Thus, both types of models demonstrate the degradation of thermal stability in case of defects, but the response to defects varies. PFU 040 p08 is prone to the formation of extreme local peaks in specific areas (position # 11), while

PFU 035 p03 is characterized by more uniform but less intense temperature growth.

It is important to note that in the PFU 035 p03 model, longitudinal castellation of W tiles was additionally made in a 1:1 ratio for each tile with a gap thickness of 0.3 mm. This design solution has an additional effect on the thermal characteristics:

1. Castellation promotes smoothing of the temperature peaks in the defect zones.

2. Total surface heating remains consistent with that of the PFU 040 p08 model.

These observations confirm that the longitudinal castellation of the tiles can be an effective measure to reduce local temperature overheating in case of defects in joints.

Data analysis makes it possible to identify several factors which may explain the observed discrepancies between the calculation and the experiment:

1. The complexity of accurate simulation of the thermal contact in the defect zones, particularly at the heat loads exceeding 2 MW/m^2.

2. Possible differences between the actual properties of materials and their theoretical properties used in the calculations.

3. Additional factors affecting the heat transfer in the actual conditions which are not fully taken into account in the calculation models (e.g., nonuniform cooling water flow, transient thermal processes).

These discrepancies underline the importance of the experiment on the calculation models and the need for their further improvement to estimate the thermal characteristics of the components with defects more accurate.

With an increasing heat load, the efficiency of the cooling system with the specified parameters (water flow rate G = 1.84 kg/s, inlet pressure P_{in} = 39 bar, inlet temperature T_{in} = 70 °C) changes unevenly:

1. At the heat loads 1–2 MW/m^2, the cooling system efficiently copes with the heat removal both in the models without defects and in the models with defects as evidenced by relatively small differences in the temperatures.

2. At the heat loads greater than 3 MW/m^2, the cooling efficiency in the defect zones decreases noticeably, which results in the formation of significant temperature gradients.

This observation is of great practical importance for the development of the cooling systems for the components operating under high heat loads and emphasizes the necessity of taking into account the potential defects when calculating the cooling parameters.

7. CONCLUSION

Based on the thermal calculation results, the steady-state temperature distributions over the PFU mock-up were obtained for three versions (original with no defects, and two modified with defects) at the surface heat load on the mock-up armour from 1 to 6 MW/m^2 and at the fixed input parameters of water in the cooling channel (water flow rate per a mock-up 1.84 kg/s, inlet water pressure 39 bar (38.5 atm) and inlet water temperature 70 °C).

The steady-state temperature fields obtained based on the thermal calculation results for the specified calculation versions allow us to draw the following major conclusions:

The defects in the joints between the copper substrates of the armour and the bronze heat sink of the PFU cause a noticeable increase in the armour temperature (both local and average), which directly depends on the defect size. In particular, the maximum considered defect size is 50% of the initial joint area (in the absence of defects); and the defect of this size may cause a temperature increase up to 55% at the maximum and up to 40% at the average relative to the value for the free-of-defect model at the heat load on the armour up to 6 MW/m^2.

The maximum temperature of the armour does not exceed 1200 °C for all examined calculation versions, i.e., at the heat load on the armour up to 6 MW/m^2 and the defect size up to 50% of the joint area.

At the heat loads on the mock-up armour up to 4 MW/m^2, water cooling of the mock-up is carried out in the convective mode over the entire area of the cooling channel surface, i.e., without boiling; and at the heat loads greater than 4 MW/m^2, the local boiling zones occur on the cooling channel surface without transition to the critical heat flux.

Additionally, the comparison was made for the results of the thermal calculations and thermal bench tests of the mock-up according to the average temperature distributions for the enhanced heat flux tile surfaces. This comparison has shown that the calculated and experimental distributions in all considered calculation (test) versions are quite similar in shape and average temperature behavior in the longitudinal and transverse directions and at the same time have quite a lot of noticeable discrepancies in average temperature values, which are most likely due to inevitable differences in the conditions of numerical simulation and experiments.

ACKNOWLEDGEMENTS

The materials of this paper are based on the work results under Contract No. 1770641334824000019O/55-24/01 of 20.06.2024 for R&D “Development of technology and pilot production of components for the Dome and First Wall panels and performance of thermal tests of divertor elements for the ITER reactor in 2024” concluded between the Institution “Project Center ITER” and JSC “NIIEFA”.

REFERENCES

[1] N. Litunovsky, E. Alekseenko, A. Makhankov, I. Mazul, Development of the armoring technique for ITER Divertor Dome, *Fusion Engineering and Design*, 2011, vol. 86, no. 9–11, pp. 1749–1752.

[2] A.A. Rybikov, N.A. Kuznetsov, N. Litunovsky, A. Makhankov, Development and testing of the technology for coating plasma-facing components of the ITER divertor central assembly, in: *Materials of III International Conference "Problems of Thermonuclear Energy and Plasma Technology"*, Izdatelskiy Dom MEI, Moscow, 2023, pp. 93–94 (in Russian).

[3] V. Tanchuk, S. Grigoriev, A. Makhankov, K. Senik, N. Yablokov, M. Belenky, M. Blinov, M. Lebedev, B. Fokin, Experimental and numerical evaluation of IR thermography method for Final Acceptance Tests of the ITER divertor dome, *Fusion Engineering and Design*, 2014, vol. 89, no. 7–8, pp. 925–931.

[4] R. Tivey, T. Ando, A. Antipenkov, V. Barabash, S. Chiocchio, G. Federici, C. Ibbott, R. Jakeman, G. Janeschitz, R. Raffray, M. Akiba, I. Mazul, H. Pacher, M. Ulrickson, G. Vieider, ITER divertor, design issues and research and development, *Fusion Engineering and Design*, 1999, vol. 46, no. 2–4, pp. 207–220.

[5] E. Visca, F. Escourbiac, S. Libera, A. Mancini, G. Mazzone, M. Merola, A. Pizzuto, Testing of high heat flux components manufactured by ENEA for ITER divertor, *Fusion Engineering and Design*, 2009, vol. 84, no. 2–6, pp. 309–313.

[6] J. Schlosser, F. Escourbiac, M. Merola, S. Fouquet, P. Bayetti, J. Cordier, A. Grosman, M. Missirlian, R. Tivey, M. Rödig, Technologies for ITER divertor vertical target plasma facing components, *Nuclear Fusion*, 2005, vol. 45, no. 6, pp. 512–518.

[7] S.N. Mazaev, T. Gurieva, A. Lapin, A. Makhankov, V. Mirgorodsky, S. Natochev, O. Nomokonova, I. Vlasov, A. Ignatov, Laser welding of plasma facing units for ITER divertor Dome manufacturing, *2011 IEEE/NPSS 24th Symposium on Fusion Engineering*, Chicago, IL, USA, 2011, pp. 1–5.

[8] T. Hirai, V. Barabash, F. Escourbiac, A. Fedosov, L. Ferrand, S. Gicquel, T. Jokinen, V. Komarov, A. Martin, M. Merola, Design and Integration of ITER Divertor Components, *Advances in Science and Technology*, 2010, vol. 73, pp. 1–10.

[9] J. Davis, V. Barabash, L. Plöchl, K. Slattery, Assessment of tungsten for use in the ITER plasma facing components, *Journal of Nuclear Materials*, 1998, vol. 258–263, pp. 308–312.

[10] T. Hirai, F. Escourbiac, V. Barabash, A. Durocher, A. Fedosov, L. Ferrand, T. Jokinen, V. Komarov, M. Merola, S. Carpentier-Chouchana, N. Arkhipov, V. Kuznetcov, A. Volodin, S. Suzuki, K. Ezato, Y. Seki, B. Riccardi, M. Bednarek, P. Gavila, Status of technology R&D for the ITER tungsten divertor monoblock, *Journal of Nuclear Materials*, 2015, vol. 463, pp. 1248–1251.

[11] T. Hirai, K. Ezato, P. Majerus, ITER Relevant High Heat Flux Testing on Plasma Facing Surfaces, *Materials Transactions*, 2005, vol. 46, no. 3, pp. 412–424.

[12] M. Missirlian, M. Richou, B. Riccardi, P. Gavila, T. Loarer, S. Constans, The heat removal capability of actively cooled plasma-facing components for the ITER divertor, *Physica Scripta*, 2011, vol. 2011, no. T145, art. no. 014080.

[13] N. Litunovsky, E. Alekseenko, V. Kuznetsov, D. Lyanzberg, A. Makhankov, R. Rulev, Repair of manufacturing defects in the armor of plasma facing units of the ITER Divertor Dome, *Fusion Engineering and Design*, 2013, vol. 88, no. 9–10, pp. 1739–1743.

[14] P. Piskarev, R. Rulev, I.V. Mazul, A.V. Krasilnikov, A.A. Pisarev, B. Kuteev, M.S. Kolesnik, V.V. Dushik, S. Bobrov, N.V. Montak, A.A. Rybikov, T.N. Bukatin, Coatings on a First Wall Plasma-Facing Surface: Analysis and High Heat Flux Testing on the Tsefey-M E-Beam Facility, *Physics of Atomic Nuclei*, 2024, vol. 87 (suppl. 1), pp. S118–S128.

[15] A. Gervash, R. Giniyatulin, T. Guryeva, D. Glazunov, V. Kuznetsov, I. Mazul, P. Ogursky, P. Piskarev, V. Safronov, R. Eaton, R. Raffray, O.N. Sevryukov, The development of technology of Be/CuCrZr joining using induction brazing, *Fusion Engineering and Design*, 2019, vol. 146, pp. 2292–2296.

[16] P.Yu. Piskarev, I.V. Mazul, L.E. Zakharov, G.M. Tarasyuk, M.S. Kolesnik, R.V. Rulev, A.Yu. Ogursky, A.A. Gervash, V.V. Ruzanov, Yu.M. Gasparyan, A.A. Pisarev, Fabrication and thermal tests of SS/Cu bimetal plate for use in the concept of flowing liquid lithium layer in tokamak limiters and divertors, *Fusion Engineering and Design*, 2022, vol. 184, art. no. 113313.

[17] A.A. Rybikov, N.A. Kuznetsov, N.V. Litunovsky, A.N. Makhankov, P.Yu. Piskarev, A.V. Eremkin, I.P. Bogdanov, V.E. Kuznecov, A.V. Volodin, N.I. Arkhipov, Determination of maximum permissible defect during brazing of tungsten-copper armour tiles for ITER divertor dome plasma-facing units, *Problems of Atomic Science and Technology, Series Thermonuclear Fusion*, 2025, vol. 2, in press.

[18] N.V. Litunovsky, A.N. Makhankov, *Device for fixing and pressing parts during high-temperature vacuum brazing in resistance furnaces*, RU patent no. RU202604U1, 2021 (in Russian).

[19] A. Eremkin, A. Volodin, A. Kokoulin, A. Komarov, V. Kuznetsov, A. Malyshev, N. Stepanov, Test facility for experimental investigation of ITER divertor components behavior under high heat fluxes, *Problems of Atomic Science and Technology, Series Thermonuclear Fusion*, 2020, vol. 43, no. 4, pp. 5–14 (in Russian).

[20] H. Shim, J. Kim, M. Cheon, S. Pak, A comparison study on the derivation of in-structure FRS during seismic events for application of ITER upper port 18, *Fusion Engineering and Design*, 2023, vol. 191, art. no. 113771.

[21] G. Aiello, M. Gagliardi, A. Meier, G. Saibene, T. Scherer, S. Schreck, P. Spaeh, D. Strauss, A. Vaccaro, ITER Torus Diamond Window Unit: FEM analyses and impact on the design, *IEEE Transactions on Plasma Science*, 2019, vol. 47, no. 7, pp. 3289–3297.

[22] C. Vidal, R. Luis, B. Pereira, R.B. Ferreira, B. Gonçalves, S.B. Korsholm, A. Lopes, E.B. Klinkby, E. Nonbøl, M. Jessen, M. Salewski, J.J. Rasmussen, B. Lauritzen, A. Larsen, Thermo-structural analyses of the in-vessel components of the ITER collective Thomson scattering system, *Fusion Engineering and Design*, 2019, vol. 140, pp. 123–132.

[23] D.M. Bachurina, P.V. Morokhov, R.S. Rasskazov, O.N. Sevryukov, B.A. Kalin, Effect of beryllium on the morphology of initial ingots and the structural phase state of fast-quenched STEMET 1108 brazing alloy ribbons, Tsvetnye Metally, 2022, no. 10, pp. 66–71 (in Russian).

[24] B.A. Kalin, A.N. Suchkov, V. Fedotov, O.N. Sevryukov, A.A. Ivannikov, A.A. Gervash, Brazing of Be with CuCrZr-bronze using copper-based filler metal STEMET, *Nuclear Materials and Energy*, 2016, vol. 9, pp. 388–393.

УДК 621.039.634

Влияние дефектов паяного соединения на работоспособность обращенных к плазме элементов центральной сборки дивертора токамака ИТЭР

А.А. Рыбиков [1,2], А.В. Еремкин [1], А.О. Комаров [1], В.Е. Кузнецов [1], А.В. Володин [1], П.Ю. Пискарев [1], И.П. Богданов [1], В.Н. Танчук [1], С.А. Григорьев [1], М.В. Дорогов [2], Н.И. Архипов [3]

[1] АО «НИИЭФА», дорога на Металлострой, д. 3, пос. Металлострой, 196641, Санкт-Петербург, Россия
[2] Институт перспективных систем передачи данных, Университет ИТМО, Кронверкский пр., 49, лит. А, 197101, Санкт-Петербург, Россия
[3] Учреждение «Проектный центр ИТЭР», ул. Расплетина, д. 11, стр. 2, 123182, Москва, Россия

Аннотация. В работе представлены результаты численного моделирования и экспериментальные результаты тепловых процессов в макетах обращенных к плазме элементов (ОПЭ) центральной сборки дивертора ИТЭР. Дивертор критически важный компонент он подвергается экстремальным тепловым нагрузкам, что предъявляет высокие требования к надежности его ОПЭ. Исследование направлено на оценку влияния параметров (геометрия, размер, локализация) механических дефектов контактной зоны вольфрам медной облицовки с бронзовым теплоотводом при тепловых нагрузках q_s = 1–6 МВт/м^2. Выполнено моделирование методом конечных элементов конфигураций ОПЭ с дефектами, различной формы и размеров. Результаты сопоставлены с экспериментальными данными тепловых испытаний. Установлено, что увеличение размера дефекта приводит к росту температуры облицовки: при максимальном дефекте (50% площади зоны соединения) локальная температура возрастает на 55%, средняя – на 40% (q_s = 6 МВт/м^2). Форма дефекта (прямоугольная/треугольная) оказывает незначительное влияние: отклонения не превышают 1,4% для максимума и 10% для средних значений. Продольная кастелляция (электроэрозионный рез) плиток в модели может вносить влияние в распределение температур. Максимальная температура на поверхности облицовки во всех вариантах не превысила 1200 °C. При нагрузках ≤ 4 МВт/м^2 охлаждение остается конвективным, при более высоких нагрузках возникают локальные зоны кипения без перехода в кризис теплообмена. Сравнение результатов расчетных и экспериментальных данных выявило схожесть распределений температур.

Ключевые слова: центральная сборка дивертора; обращённый к плазме элемент; механический дефект пайки; тепловые испытания; кастеляция